16

Use and Limitations of Single- and Multi-Mode Optical Fibers for Exoplanet Detection

Julien F.P. Spronck, Debra A. Fischer
and Zachary A. Kaplan
Yale University
USA

1. Introduction

Optical fibers are of a great importance in diverse areas of modern observational astronomy. Particularly, in the field of exoplanet detection, they have become an essential part of most current and future instruments because of their filtering and stabilizing capability.
In this chapter, we will discuss the use of optical fibers and some limitations in two exoplanet detection methods: nulling interferometry (Section 2) and the radial velocity method (Section 3). We will present simulations, experiments and observations that demonstrate improvements of the instrument performances in the field of exoplanet detection due to the use of optical fibers, as well as some of their limitations.

2. Single-mode fibers in nulling interferometry

Nulling interferometry is a direct exoplanet detection method, aimed at the detection of an Earth-like planet around a Sun-like star (Bracewell, 1978; Colavita et al., 2010; Mennesson et al., 2011). It consists in combining light from several telescopes in such a way that a quasi-perfect destructive interference occurs for the star light. In such an instrument, the light coming from a potential planet orbiting the star would experience a (partially) constructive interference because of the optical path differences between the arms of the interferometer for an off-axis point source (i.e. the planet).
Single-mode fibers are used in all state-of-the-art wide-band nulling interferometers because they provide natural wavefront filters, essential for a quasi-perfect destructive interference (Mennesson et al., 2002; Wallner et al., 2003).
In addition to canceling the light from the star and thus making possible direct detection of planets, nulling interferometry should also offer the possibility to obtain spectral information from the planet if destructive interference can be achieved simultaneously for all wavelengths in a wide spectral band (typically from 5-18 μm would be the optimal wavelength range because it is where the brightness ratio between the star and the planet is minimal)(Angel et al., 1986; Angel & Woolf, 1997). To realize that, very stringent requirements must be fulfilled in terms of amplitude, phase and polarization of the beams to be combined for all wavelengths. Most nulling interferometers use achromatic phase shifters (Rabbia et al., 2003) to create an on-axis destructive interference independent of the wavelength and must

also use an achromatic amplitude-matching device. The use of single-mode fibers in a nulling interferometer can affect this achromaticity condition because the coupling of light into a waveguide is wavelength-dependent. This coupling can therefore chromatically affect both the amplitude and the phase of the beam.
In particular, two beams with slightly different wavefronts will have different wavelength-dependent coupling efficiencies. This results in different wavelength-dependent amplitudes and phases, which will limit the performance of the interferometer. A measure for this performance is called the rejection ratio: it is the ratio between the intensities corresponding to constructive and destructive interferences.
In this section, we will calculate the wavelength-dependent coupling efficiencies of aberrated beams into a single-mode fiber and analyze the influence of aberrations on the rejection ratio and therefore on the performance of the nulling interferometer. From these results, we will quantitatively derive the wavefront quality required to allow the detection of Earth-like planets. We will then show that amplitude, optical path difference and dispersion corrections can be used to reduce the effect of induced wavelength-dependent coupling efficiencies and relax the tolerances on optical quality.

2.1 Definitions

Let us consider the case of a two-beam nulling interferometer. We will assume that a perfectly achromatic π-phase shift has been introduced between the beams in order to get destructive interference for all wavelengths.
Each of the beams i ($i = 1$ or 2) has a distorted wavefront W_i, which can be described in terms of normalized Zernike polynomials (Noll, 1976),

$$W_i(x,y) = \sum_j a_j^{(i)} Z_j(x,y). \tag{1}$$

In this representation, each polynomial represents an aberration and the coefficient $a_j^{(i)}$ gives the RMS contribution of the corresponding aberration to the total wavefront.
As explained in Section 2, the beams are then focused onto a single-mode fiber that acts as a wavefront filter. Indeed, the field at the output of the fiber is given (all losses neglected) by the fundamental mode of the fiber, multiplied by a complex factor ξ_i called the complex coupling efficiency that represents the part of the field that is coupled in the fiber (Mennesson et al., 2002; Wallner & Leeb, 2002). This holds for any incoming field and therefore, all wavefront distortions are taken care of by the optical fiber. However, different wavefronts will induce different (wavelength-dependent) coupling efficiencies and this will limit the rejection ratio.
The field in the focal plane is given by the Fourier transform of the field in the entrance pupil,

$$E_i(X,Y,\lambda) = \iint \exp\left[j\frac{2\pi}{\lambda}W_i(x,y)\right] \exp\left[-j\frac{2\pi}{\lambda f}(xX+yY)\right] dxdy, \tag{2}$$

where λ is the wavelength, f the focal length of the focusing optics, (X,Y) and (x,y) are respectively the coordinates in the focal plane and in the entrance pupil plane.

The complex coupling efficiency ξ_i of beam i is then given by the overlap integral between the incident field E_i and the fundamental mode of the fiber F_0,

$$\xi_i(\lambda) = \frac{\iint E_i(X,Y,\lambda)F_0^*(X,Y,\lambda)dXdY}{\iint |F_0(X,Y,\lambda)|^2 dXdY}, \tag{3}$$

where * denotes the complex conjugate.
The rejection ratio R is the ratio between intensities corresponding to constructive and destructive interferences. Therefore, we have

$$R = \frac{\int |\xi_1(\lambda) + \xi_2(\lambda)|^2 d\lambda}{\int |\xi_1(\lambda) - \xi_2(\lambda)|^2 d\lambda}. \tag{4}$$

2.2 Influence of each aberration on the rejection ratio

We consider a spectral band going from 500 to 650 nm. This spectral band was chosen to match an existing experimental set-up. We will first assume that one of the beams has a perfect plane wavefront ($a_j^{(1)} = 0$ for all j), while the second wavefront is distorted. In this first simulation, we will study the influence of each aberration separately by setting the coefficient $a_j^{(2)} = 30$ nm (wavefront at roughly $\lambda/20$ RMS) and calculate the rejection ratio as a function of the Zernike index j (each index represents a different type of aberration). The results are depicted in Figure 1 (black squares).
We see a "wave" pattern in the rejection ratio as a function of Zernike index. Each of these waves corresponds to a different radial order of the Zernike polynomials. For each radial order, the rejection ratio is minimal for zeroth azimuthal order (radially symmetric) and increases with azimuthal order (towards higher spatial frequencies). The rejection ratio also increases with radial order, since the fiber is less sensitive to high spatial frequencies.
The aberrated wavefront introduced amplitude and phase mismatches between the two beams. There are therefore a few corrections that we can apply to improve the rejection ratio. We can first use an achromatic intensity-matching device, e.g. a knife-edge (which is achromatic at first order) to match the global intensities of the two beams (see Figure 1, blue diamonds). Then, we can use an optical delay line to match the optical path differences (OPD) between the beams (see Figure 1, red stars). Finally, we can compensate for dispersion differences by adding glass plates with variable thicknesses (see Figure 1, magenta crosses) (Spronck et al., 2008; Spronck et al., 2009).
We see that OPD and dispersion compensation only improves the rejection ratio for the fourth (defocus), the twelfth (spherical aberration) and the twenty-fourth (6th order spherical aberration) Zernike polynomials. Indeed these polynomials have a zero azimuthal frequency (radial symmetry) and we can show that the coupling efficiencies corresponding to non-zero azimuthal frequencies are real. Therefore, for these aberrations, no phase corrections can increase the rejection ratio, only the amplitude correction can. Note that the limitation of the rejection ratio is due to a wavelength-dependent amplitude mismatching, for which we cannot easily compensate. Therefore, these results will strongly depend on the width of the spectral band.

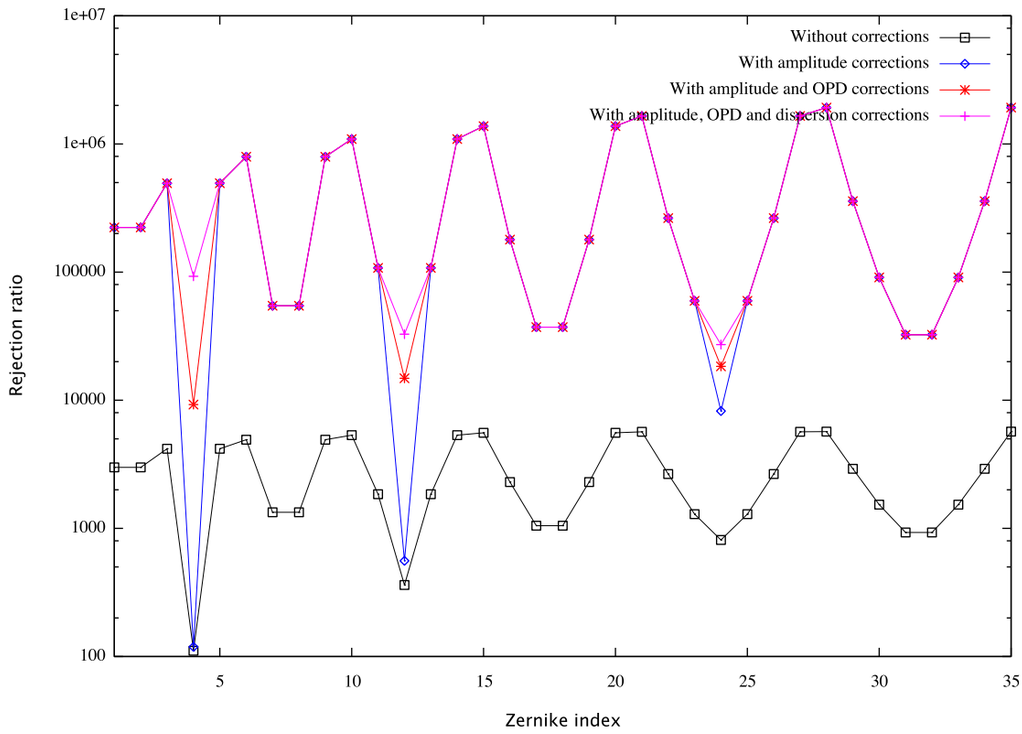

Fig. 1. Rejection ratio as a function of Zernike index when $a_j^{(1)} = 0$ for all j and $a_j^{(2)} = 30$ nm (black squares). The blue diamonds correspond to the rejection ratio after an achromatic intensity matching. For the red stars, the OPD have been matched (additionally to the intensity matching). The magenta crosses corresponds to rejection ratio with intensity, OPD and dispersion correction.

2.3 Rejection ratio with randomly chosen wavefronts

In this other simulation, we randomly chose the coefficients $a_j^{(1)}$ and $a_j^{(2)}$ for both wavefronts in such a way that these wavefronts have a standard deviation of 30 nm RMS ($\lambda/20$) (see Figure 2). We found the average rejection ratio with such wavefronts after 35 simulations is of the order of 10^3 without corrections and 10^6 with amplitude, OPD and dispersion corrections. We then repeated this simulation with different wavefront standard deviations and plotted the average rejection ratio as a function of RMS wavefront quality (see Figure 3). From this, we derive that the necessary RMS wavefront quality to obtain a 10^6-rejection ratio is 40 nm RMS ($\lambda/15$). This means that the surface figure of the optics (we only considered here the case of reflective optics) should be better than $\lambda/30/\sqrt{N_{opt}}$ where N_{opt} is the total number of surfaces encountered by the beams.

It is important to realize that these results highly depend on the desired spectral band and cannot directly be translated in a general requirement. However, this is meant to indicate the limitations of single-mode fibers in nulling interferometry. Note also that it will be easier to meet the requirements in the IR where nulling interferometers mainly perform.

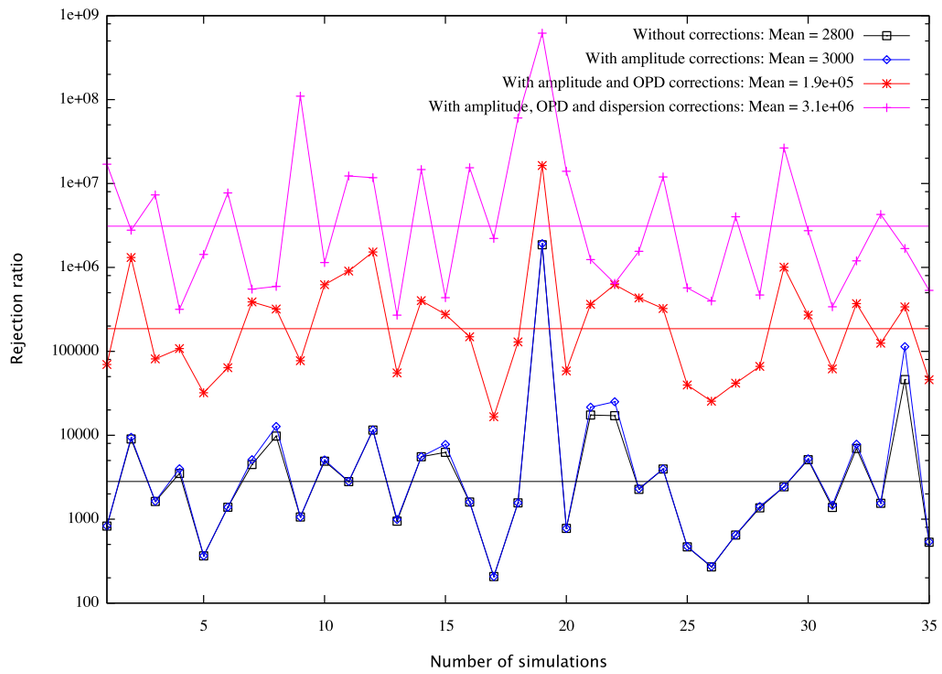

Fig. 2. Rejection ratio for two beams with randomly chosen wavefronts that have a standard deviation of 30 nm RMS.

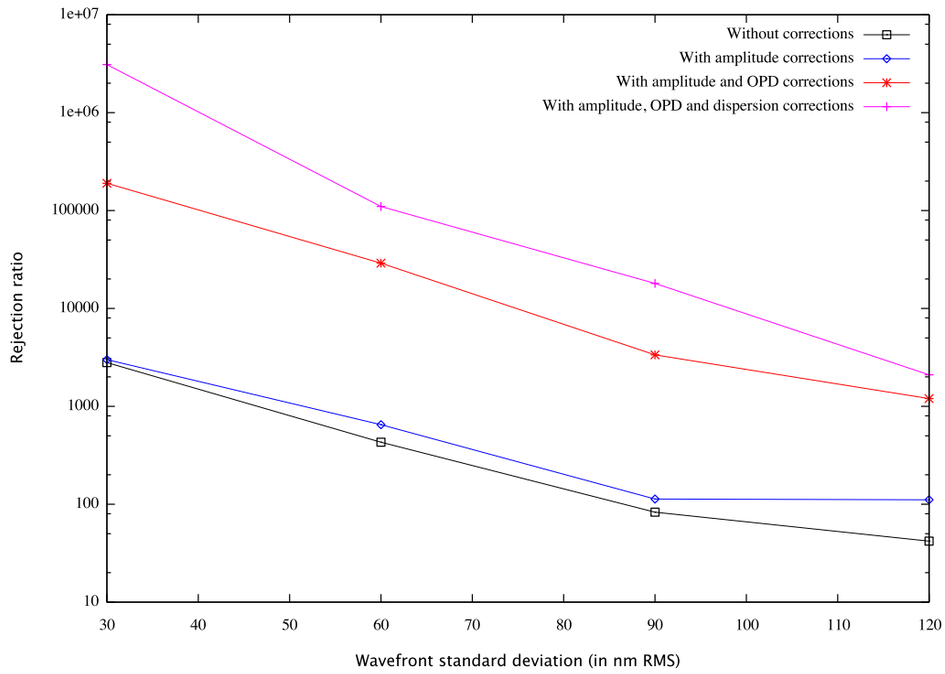

Fig. 3. Rejection ratio as a function of RMS wavefront quality.

3. Multi-mode fibers for high-precision radial velocities

Since the discovery of the first exoplanet by Mayor & Queloz (1995), more than 500 planets have been found using the radial velocity method. Currently, the state-of-the-art spectrometers, such as HARPS (Mayor et al., 2003) on the 3.6-m telescope in La Silla and HIRES on Keck I (Vogt et al., 1994), typically achieve precisions of 1-3 m s^{-1} (Howard et al., 2010; Mayor & Udry, 2008). This only permits the detection of planets with amplitudes larger than the measurement errors, typically Super Earth or Neptune-mass planets in relatively short period orbits, or more massive Jupiter-like planets out to several AU. The detection of true Earth analogs requires Doppler precisions on the order of 10 cm s^{-1}, corresponding to spectral line shifts across one ten-thousandth of a pixel. Further complicating the analysis, the periodicity of this shift occurs over time scales of months or years for the most interesting planets in the so-called habitable zone. This top level requirement for a measurement precision of 10 cm s-1 leads to the demand for an instrument that exceeds the stability of current instruments.

In order to reach the desired precision, we must reduce errors in the model of the instrumental profile, which cross-talk with our measurement of the Doppler shift. In older spectrographs, the starlight is coupled from the telescope to the instrument using a narrow slit. However, the slit illumination is rapidly varying because of changes in seeing, focus and guiding errors. Changes in slit illumination affect the spectrum in two ways. Since the spectral lines are direct images of the slit, changes in slit illumination yield changes in the shape of the spectral lines. Additionally, variations in slit illumination can result in changes in the illumination of the spectrograph optics. This will in turn introduce different aberrations, which will change the instrumental response. Mathematically, these two effects are modeled simultaneously by convolving the spectrum with the instrumental profile (IP), in such a way that any variability impedes our ability to recover Doppler shifts with the desired precision. If the instrumental profile were unchanging, variations in the final extracted spectrum would be dramatically reduced. Thus, instrumental profile stability has become a focus of current instrumentation work.

Optical fibers provide an excellent way to reduce variability in the illumination of the spectrograph. Fibers have been used since the 1980's to couple telescopes to high-precision spectrographs (Heacox & Connes, 1992). The throughput of fibers was initially low, however, they offered unprecedented convenience in mechanical design. The attribute of fibers that is particularly important today for high-precision Doppler measurements is the natural ability of optical fibers to scramble light (Barden et al., 1981; Heacox, 1980; 1986; 1988) and produce a more uniform and constant output beam. Because light from the telescope must be efficiently coupled into the fiber, the fiber diameters must match the typical image size (generally 100 microns or more), so multi-mode fibers are required.

Other sources of errors come from environmental changes within the spectrograph. Temperature, pressure or mechanical variations cause the spectrum to shift and to change. These errors will not be solved by replacing the slit by a fiber.

3.1 Laboratory characterization

We have carried out laboratory measurements to better understand scrambling properties of fibers with different geometries (circular, square, octagonal), different lengths, and different fiber diameters. While testing these fibers, we have noticed that the optical properties vary

widely from fiber to fiber. This is even true for supposedly identical commercial fibers from the same manufacturer and same production batch.
At an observatory, the illumination of the fiber will vary due to guiding, focusing errors and seeing changes. To characterize the scrambling properties of the fiber under similar conditions, we scan the incoming beam across the fiber and examine the output beam.
As described by Hunter & Ramsey (1992), two characteristics are of importance when it comes to the output beam: the far-field and the near-field patterns. The far-field is the cross-sectional intensity distribution of the diverging beam. The far-field will be projected onto the collimator, the grating and the rest of the spectrograph optics. Variations in the far-field will therefore cause different parts of the grating and the optics to be illuminated. This will in turn introduce different aberrations, which will change the instrumental profile. The near-field pattern is the intensity distribution across the output face of the fiber. The spectral lines are direct images of the fiber output face, so variations in the near-field pattern are also important in the stability of the final spectrum. Commonly (but erroneously), the term near-field is used to describe the image of the output face of the fiber by an optical system. We will adopt this definition throughout this chapter.

3.1.1 Experimental set-up

The set-up used for the fiber characterization measurements is depicted in Figure 4.
We focus the light from either a green He-Ne laser or a LED onto a single-mode fiber that is used to create a star-like point source. Light coming from the single-mode fiber is then collimated (by lens L_2) and re-focused (by lens L_3) onto the test multi-mode fiber. Light reflected from the fiber front surface is re-directed using a beam-splitter and re-imaged onto a CCD (CCD_1) to check the alignment of the beam with respect to the fiber front surface. A translation stage allows us to move the fiber with respect to the incoming beam and therefore simulate guiding errors. Light coming out of the test fiber is then collimated (by lens L_7) and re-focused (by lens L_5) onto a CCD (CCD_2). Lens L_6 moves in and out of the light path to enable measurements of the near-field (out) and the far-field (in) patterns.

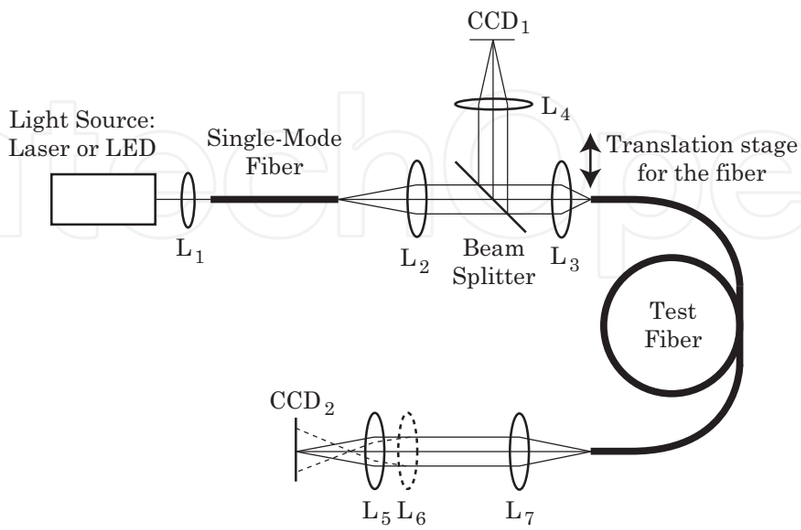

Fig. 4. Schematic drawing of our set-up.

3.1.2 Scrambling versus fiber length

We first measured the amount of scrambling as a function of fiber length. All fibers used in this test were 50-micron fibers from Polymicro (FBP050070085) with lengths of 5, 20 or 40 m. We used a similar set-up as described in Section 3.1.1. A green He-Ne laser was coupled into the single-mode fiber. A couple of lenses were used to re-image the single-mode fiber onto the test fiber. The used imaging system was not of very high quality, so that the spot size was a significant fraction of the fiber core.

For this experiment, we inserted a mirror on a kinematic mount between the two lenses and tilted it to scan the image across the fiber face and simulate guiding errors. The far-field pattern was recorded as a function of mirror tilt (or equivalently of beam position on the fiber). To eliminate the speckle pattern caused by modal interference, we agitated the test fiber.

Figure 5 depicts the far-field patterns as a function of beam position on the fiber for three different fiber lengths (5, 20 and 40m). The left columns corresponds to input that was well centered on the fiber. In the right columns, the beam is increasingly displaced from the fiber center. For the 5-m fiber, we clearly see rings when moving away from the center, which become dominant rather quickly. The 5-m fiber quickly develops a ring pattern. Rings are also seen for the 20-m fiber, but not until the image is much further displaced from the center. No ring pattern appears for the 40-m fiber; the far-field distribution seems almost independent of the spot position.

Any type of variation in the far-field pattern is undesirable since it will induce variations in the illumination of the grating and spectrograph optics that will cause varying instrumental profile.

The rings occur because light is propagating through the cladding: they only appear when the spot was large enough to overlap with the cladding (i.e., when the spot was slightly off-center). Because light does not propagate very well in the cladding, there is a dependence on fiber length and the 40-m fiber is long enough that this pattern is not seen in the output beam.

These measurements were confirmed by measuring three fibers of each length. They all exhibited the same behavior.

There are two important consequences of these measurements. First, longer fiber will be better for scrambling. On the other hand, longer fiber will have a lower throughput. For example, the Polymicro FBP fibers have 15 dB/km losses due to absorption at 500 nm. For a 5-m fiber, that gives a throughput of 99 % for a 5-m fiber and 90 % for a 40-m fiber. A trade-off between scrambling and throughput is needed given a specific application.

The second consequence is that if good scrambling is desired, the cladding should never be illuminated. Cladding illumination can be avoided by appropriate masking (in the fiber input plane or more easily, in an intermediate focal plane). The mask alignment can be critical.

3.1.3 Scrambling with circular fibers

In this test, we used the set-up depicted in Figure 4. A green LED (50-nm FWHM) was used as light source. In terms of coherence length, a standard He-Ne laser would be more appropriate than the LED for very high-resolution spectrographs. However, because of its low coherence, the LED makes it possible to measure reproducible and precise fiber outputs without agitating the fiber.

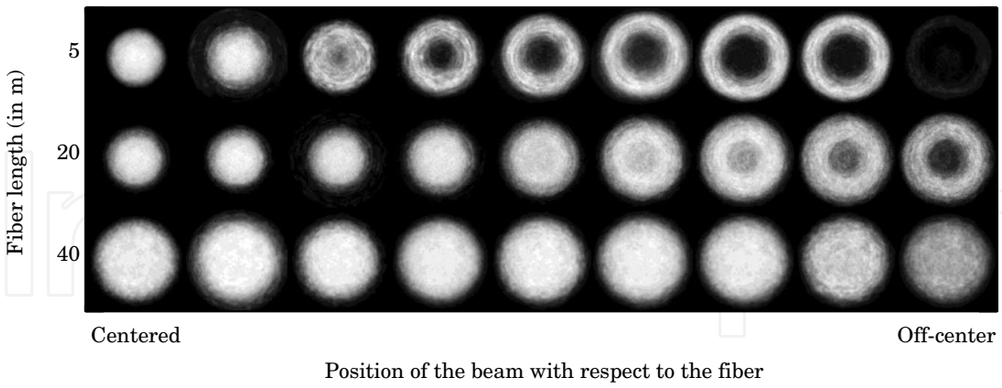

Fig. 5. Scrambling of 50-micron fibers of various lengths

The single-mode fiber was re-imaged onto the test multi-mode fiber using a pair of diffraction-limited aspheric lenses. This time, the resulting spot onto the test fiber was much smaller than the fiber. Using a commercial camera, we imaged the input face of the test fiber and the spot. This way we could carefully position the spot with respect to the fiber and we could also make sure that the test fiber was exactly in the image plane (and thus the spot was well in focus when entering the fiber).
We scanned the spot with respect to the fiber by moving the fiber (which was on a differential screw stage with a precision of 1 μm). For every fiber position, we checked the spot position with the camera. We then recorded both far-field and near-field patterns for every fiber position.
Figure 6 shows the far-field (top row) and near-field (bottom row) as a function of fiber position (from cladding to cladding) for a 15-m long 100-micron Polymicro fiber (FBP100120140). The far-field pattern shows strange non-radially symmetric structures but both far-field and near-field distributions are nearly independent of fiber position. However, looking closer at the near-field (see Figure 7), systematic variations can be seen for different fiber positions. This position memory is evidence of non-perfect scrambling by the fiber and will limit the instrumental profile stability of a high-resolution spectrograph, since guiding errors will directly translate into variations in near-field patterns.

3.1.4 Scrambling with octagonal fibers

It has been suggested that fibers with different geometries (square, hexagonal, octagonal) were better scramblers and were therefore more suitable for high-precision radial velocities (Avila et al., 2010; Chazelas et al., 2010). We purchased 20-m octagonal fibers from CeramOptec with a 200-micron octagonal core and a 672-micron round cladding.
We repeated the measurements presented in Section 3.1.3. Figure 8 summarizes the results. The top row is the far-field, the middle row is the near-field and the bottom row shows the spot position across the input fiber face.
The far-field is better behaved in terms of symmetry than it was for the circular fiber but is not as position independent for the octagonal fiber. On the other hand, the near-field (see

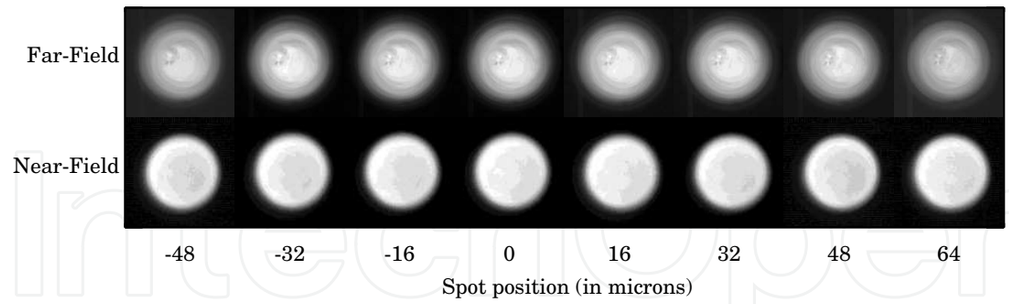

Fig. 6. Scrambling of a circular fiber.

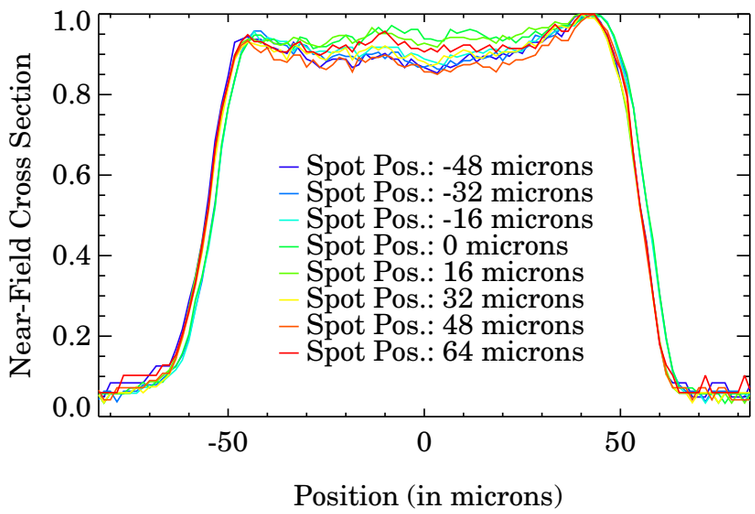

Fig. 7. Scrambling of a circular fiber.

Figure 9) shows no systematic variations and seem independent of fiber position (within the measurement precision).
The fact that the near-field is so independent on beam position is very encouraging for use in high-resolution spectrographs, as it probably yields a very stable instrumental profile. In contrast, the far-field is not as good and depending on the local quality of the spectrograph optical components, can contribute to some variations in instrumental profile.

3.2 Results at Lick observatory

In 2009, we have installed a fiber feed for the Hamilton spectrograph on the 3-m telescope at Lick Observatory (Spronck et al., 2010). The key results are presented in this section.

3.2.1 Comparison between slit and fiber using the Hamilton spectrograph

In August 2010, extensive tests were carried out to quantify the improvement in instrumental profile stability brought by the fiber scrambler and to identify the remaining sources of error.

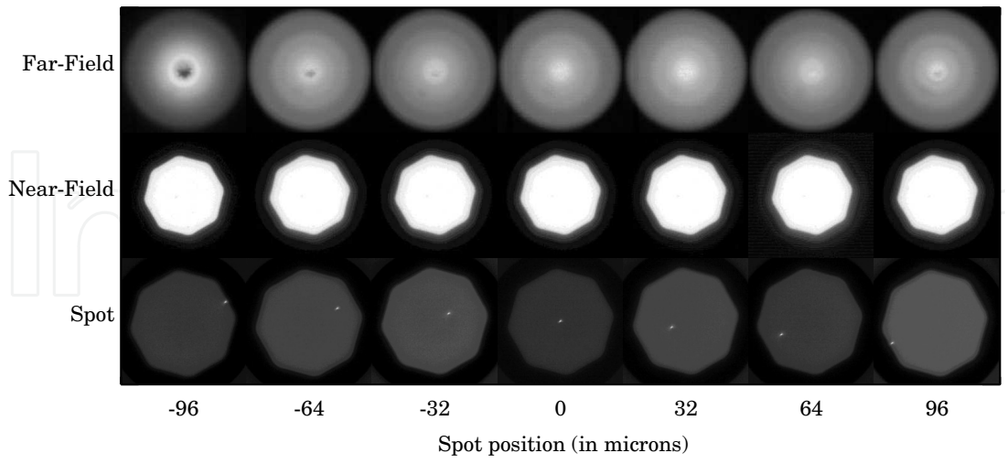

Fig. 8. Scrambling of an octagonal fiber.

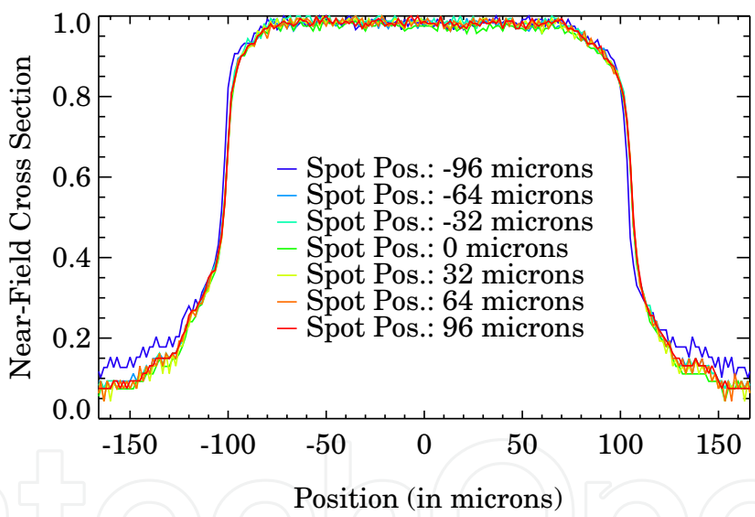

Fig. 9. Scrambling of an octagonal fiber.

Observations of stars with known constant radial velocity were made on two consecutive nights. The weather and seeing conditions were nearly identical for both nights. The fiber scrambler was installed for the first night, and the regular observing slit (640 μm wide) was used on the second night.

On both nights, an iodine cell was used. As starlight passes through the cell, the molecular iodine imposes thousands of absorption lines in the stellar spectrum. We use an extremely high resolution ($R \approx$ 1,000,000), high SNR Fourier Transform Spectrum (FTS) of the iodine cell to model the instrumental profile, which when convolved with the product of the stellar spectrum and the iodine FTS spectrum reproduces the observed spectrum. The instrumental

profile must be modeled for small wavelength segments of the echelle spectrum to account for 2-D spatial variations. Although there are some asymmetries in the wings of the IP, a single Gaussian gives, for our purpose, a reasonable fit to the composite IP. We fitted a Gaussian to the instrumental profile for each of the spatial regions on the CCD and calculated the average full-width half maximum (FWHM) of the Gaussian across the entire detector (iodine region). Figure 10 depicts the evolution of the average FWHM for the slit observations (blue squares) and for the fiber observations (red filled circles) through time. The abscissa in this plot is the sequential observation number through the night. The time-dependence variation of the IP for the slit observations (blue squares) is quite dramatic. For both nights, the same sequence of observations were taken: a set of B stars, 50 observations of the velocity standard star HD 161797, a second set of B stars, 50 observations of the velocity standard star HD 188512 and a third set of B stars.

The smooth functional dependence on time for slit observations strongly suggests that the dominant factor in the instrumental profile variation is the changing illumination of the slit due to monotonic changes in seeing or tracking through different hour angles (which might result in different input angles into the fiber). The peak-to-valley (PTV) amplitude of the variation is about 8% throughout the night.

Figure 10 also shows significant improvement in instrumental profile stability due to the fiber scrambler (red solid dots). However, there is still a slight linear (upward) trend in the fiber data (1%-2% PTV), indicative of incomplete scrambling with the fiber. After removing the linear trend, the residual fluctuation is of the order of 1% PTV.

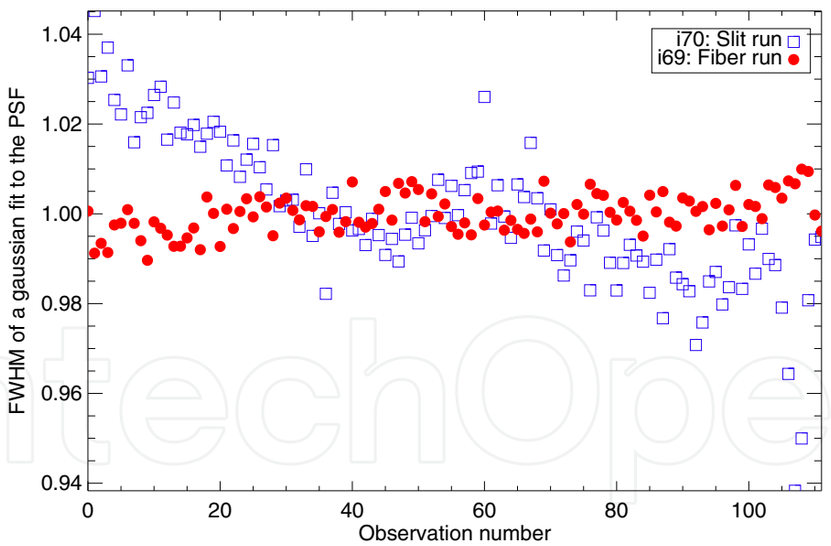

Fig. 10. Average FWHM of a Gaussian fit to the instrumental profile for all observations during Night 1 using the fiber (red filled circles) and Night 2 using the slit (blue squares).

3.2.2 Results with a double scrambler using the Hamilton spectrograph

In August 2010, a double scrambler (Avila, 1998; Hunter & Ramsey, 1992) was designed and built. In this double scrambler, a ball-lens transforms the image of the fiber end in a pupil that is then injected into a second fiber. The light from the second fiber is then sent to the

spectrograph. Because of time constraints, the double scrambler was not optimized and as a consequence, the throughput when used in the Hamilton spectrograph was rather low (15% as opposed to 55-60% with one fiber only).
The double scrambler test consisted in taking alternative sets of five B-star observations with the regular fiber scrambler (one fiber only) and with the double scrambler throughout the same night. For each observation, we calculated the instrumental profile for each region of the CCD and fitted it with a Gaussian. We then calculated the average FWHM of the fit across the entire detector.
Figure 11 depicts the evolution of the average FWHM for the single fiber observations (blue) and for the double scrambler observations (red) through the night. Different symbols correspond to different sets of B stars. Even though the scale is different from Figure 10 (with the slit observations), we can still see a linear trend in the fiber data in Figure 11, indicating imperfect fiber scrambling. In this case, the amplitude of the variation is about 3%.
The IP obtained with the double scrambler is significantly more stable throughout the night, with no significant (above errors) systematic trend.
Instrumental noise can be broken down into two main components: errors due to coupling of the light to the instrument (varying fiber illumination due to guiding, tracking, seeing and focusing) and environmental instability (mechanical, temperature or pressure). The double scrambler results prove that coupling errors are the dominant source of instrumental noise.
Residual fluctuations from observation to observation have an amplitude of 1%, which is large for precise radial velocities. The source for these fluctuations has not yet been identified but possible culprits include modal noise in the fiber, photon noise and modeling errors. We do not expect the environmental instability to be responsible for residual fluctuations because of the short time scale of the variability.

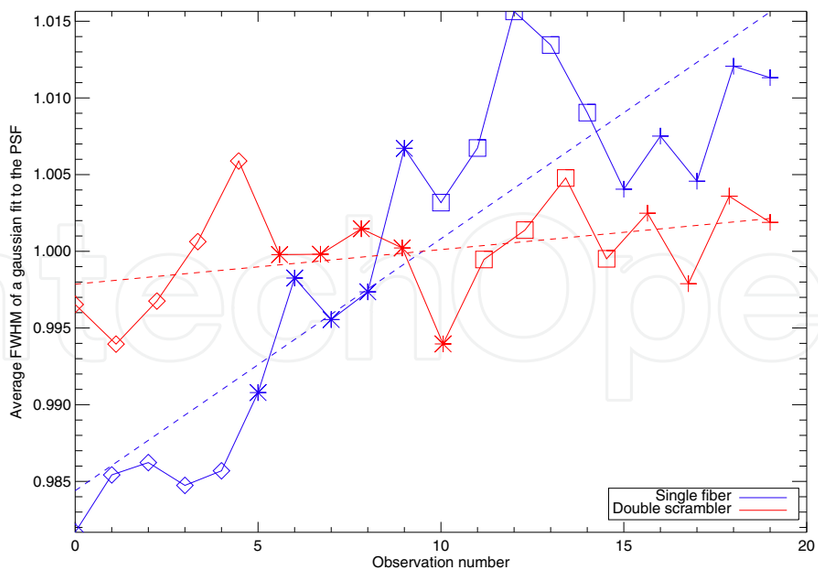

Fig. 11. Average FWHM of a Gaussian fit to the instrumental profile for B-star observations taken with the fiber (blue) and with the double scrambler (red). All observations were taken during the same night alternating with the fiber and with the double scrambler.

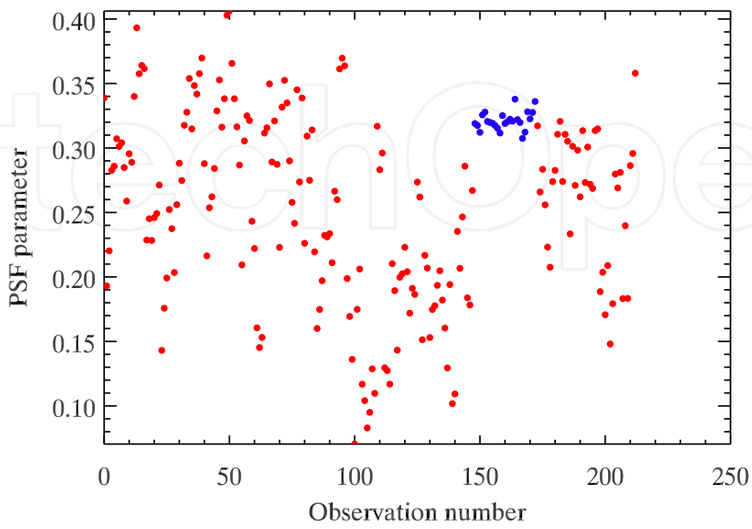

(a)

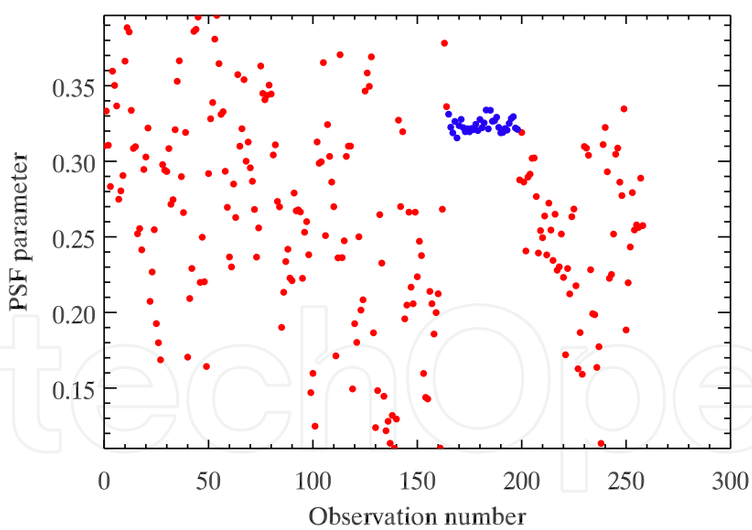

(b)

Fig. 12. Instrumental profile parameters for all HIRES observations of (a) HD 26965 and (b) HD 32147. Red dots correspond to slit observations and blue dots correspond to fiber observations.

3.3 Results at Keck observatory

During the last week of September 2010, we repeated the tests performed at Lick Observatory at the Keck telescope using the HIRES spectrograph. The larger aperture telescope at Keck helped to keep the exposure times short so that a large data set could be acquired and so that barycentric errors were minimized. We designed and built a prototype fiber scrambler with a 200-micron 20-m Polymicro fiber

We collected data on two nights; on 30 September 2010, we used the fiber scrambler and on 1 October 2010, we obtained a similar set of data with the usual slit. We observed sets of 25 observations for the standard stars HD 26965 and HD 32147. Figure 12(a) and (b) depict one of the parameters used to model the instrumental profile for all existing observations of (a) HD 26965 and (b) HD 32147. The red filled circles correspond to slit observations and exhibit an RMS scatter of 0.066 for HD 32147, while the fiber observations for the same star (blue filled circles) exhibit a dramatically reduced RMS scatter of 0.0044, demonstrating a factor of 15 improvement in the IP stability.

4. Conclusion

In the fist part of this chapter, we have studied the performances of a two-beam nulling interferometer with distorted wavefronts. We have studied the influence of each individual aberration and we have seen that aberrations will induce phase and amplitude mismatches between the beams that can partially be compensated. Unfortunately the wavelength-dependence of these mismatches will limit the rejection ratio. We have seen that the interferometer will be more sensitive to lower order aberrations (both radial and azimuthal orders). In particular, aberrations that will mostly limit the rejection ratio are radially symmetric aberrations (such as defocus, spherical aberration and sixth order spherical aberration). For the considered spectral band (500-650 nm), we quantified the wavefront and surface quality needed to have a rejection ratio of 10^6. The quality of the wavefront should be better than $\lambda/15$ RMS. This result depends on the width of the spectral band. Even though single-mode fibers are essential parts of nulling interferometers, they are not perfect modal filters and will eventually limit the performances of the instrument if care is not taken in the optical design.

In the second part of this chapter, we have characterized the scrambling properties of multi-mode fibers as a function of length and cross-sectional geometry. We conclude that longer fibers perform better in terms of scrambling (but have lower throughput) because light in the cladding will not propagate efficiently. We also conclude that the best scrambling is achieved when the cladding is not illuminated. We see evidence of non-perfect scrambling in the near-field of the circular fiber, while the octagonal fiber has a very well-behaved near-field. This implies that the octagonal fiber should therefore yield a very stable instrumental profile. However, we find that the far-field of the octagonal fiber is not as good and therefore octagonal fibers will only be helpful if the grating and other spectrograph optics have excellent optical quality.

To summarize, in order to measure spectral line shifts smaller than one ten-thousandth of a pixel and stable for many months, we must reduce errors in our instrumental profile, which cross-talks with our measurement of the Doppler shift. The instrumental noise can be broken down in coupling errors (slit or fiber illumination) and environmental instability. These results show that coupling errors are the dominant source of instrumental noise. We show that double

scrambler observations have a more stable IP than fiber observations, which have a more stable IP than slit observations. The double scrambler data still has residual RMS scatter. The source of this has not yet been identified but is likely to be modal noise, photon noise or modeling errors. We do not expect that the residual scatter can be caused by environmental effects due to the random nature of the variability.

While some fibers are clearly better than others at scrambling light, modal noise will always limit the ability of multi-mode fibers to perfectly scramble light and therefore multi-mode fibers will produce some variability in the instrumental profile. Whether this is important or not depends on the level of precision needed in terms of radial velocities. When looking for Earth analogs, a Doppler precision of 10 cm s^{-1} or better will be required. At this level of precision, everything becomes relevant.

5. Acknowledgments

We acknowledge the support of the Planetary Society, who made possible the development and installation of the fiber feeds at Lick and Keck Observatory. We also would like to thank the National Science Foundation for their support.

6. References

Angel, J. R., Cheng, A. Y. S. & Woolf, N. J. (1986). A space telescope for ir spectroscopy of earthlike planets, *Nature* 232: 341–343.

Angel, J. & Woolf, N. J. (1997). An imaging nulling interferometer to study extrasolar planets, *The Astrophysical Journal* 475(1): 373–379.

Avila, G. (1998). Results on Fiber Characterization at ESO, *in* S. Arribas, E. Mediavilla, & F. Watson (ed.), *Fiber Optics in Astronomy III*, Vol. 152 of *Astronomical Society of the Pacific Conference Series*, p. 44.

Avila, G., Singh, P. & Chazelas, B. (2010). Results on fibre scrambling for high accuracy radial velocity measurements, *Society of Photo-Optical Instrumentation Engineers (SPIE) Conference Series*, Vol. 7735 of *Society of Photo-Optical Instrumentation Engineers (SPIE) Conference Series*.

Barden, S. C., Ramsey, L. W. & Truax, R. J. (1981). Evaluation of some fiber optical waveguides for astronomical instrumentation, *PASP* 93: 154–162.

Bracewell, R. N. (1978). Detecting nonsolar planets by spinning infrared interferometer, *Nature* 274(5673): 780–781.

Chazelas, B., Pepe, F., Wildi, F., Bouchy, F., Perruchot, S. & Avila, G. (2010). New scramblers for precision radial velocity: square and octagonal fibers, *Society of Photo-Optical Instrumentation Engineers (SPIE) Conference Series*, Vol. 7739 of *Society of Photo-Optical Instrumentation Engineers (SPIE) Conference Series*.

Colavita, M. M., Serabyn, E., Ragland, S., Millan-Gabet, R. & Akeson, R. L. (2010). Keck Interferometer nuller instrument performance, *Society of Photo-Optical Instrumentation Engineers (SPIE) Conference Series*, Vol. 7734 of *Society of Photo-Optical Instrumentation Engineers (SPIE) Conference Series*.

Heacox, W. (1980). A Optical Fiber Spectrograph Coupler, *in* A. Hewitt (ed.), *Optical and Infrared Telescopes for the 1990's*, p. 702.

Heacox, W. D. (1986). On the application of optical-fiber image scramblers to astronomical spectroscopy, *AJ* 92: 219–229.

Heacox, W. D. (1988). Wavelength-precise slit spectroscopy with optical fiber image scramblers, *in* S. C. Barden (ed.), *Fiber Optics in Astronomy*, Vol. 3 of *Astronomical Society of the Pacific Conference Series*, pp. 204–235.

Heacox, W. D. & Connes, P. (1992). Optical fibers in astronomical instruments, *A&A Rev.* 3: 169–199.

Howard, A. W., Marcy, G. W., Johnson, J. A., Fischer, D. A., Wright, J. T., Isaacson, H., Valenti, J. A., Anderson, J., Lin, D. N. C. & Ida, S. (2010). The Occurrence and Mass Distribution of Close-in Super-Earths, Neptunes, and Jupiters, *Science* 330: 653.

Hunter, T. R. & Ramsey, L. W. (1992). Scrambling properties of optical fibers and the performance of a double scrambler, *PASP* 104: 1244–1251.

Mayor, M., Pepe, F., Queloz, D., Bouchy, F., Rupprecht, G., Lo Curto, G., Avila, G., Benz, W., Bertaux, J.-L., Bonfils, X., Dall, T., Dekker, H., Delabre, B., Eckert, W., Fleury, M., Gilliotte, A., Gojak, D., Guzman, J. C., Kohler, D., Lizon, J.-L., Longinotti, A., Lovis, C., Megevand, D., Pasquini, L., Reyes, J., Sivan, J.-P., Sosnowska, D., Soto, R., Udry, S., van Kesteren, A., Weber, L. & Weilenmann, U. (2003). Setting New Standards with HARPS, *The Messenger* 114: 20–24.

Mayor, M. & Queloz, D. (1995). A jupiter-mass companion to a solar-type star, *Nature* 378: 355–359.

Mayor, M. & Udry, S. (2008). The quest for very low-mass planets, *Physica Scripta Volume T* 130(1): 014010.

Mennesson, B., Ollivier, M. & Ruilier, C. (2002). Use of single-mode waveguides to correct the optical defects of a nulling interferometer, *J. Opt. Soc. Am. A* 19(3): 596–602.

Mennesson, B., Serabyn, E., Hanot, C., Martin, S. R., Liewer, K. & Mawet, D. (2011). New Constraints on Companions and Dust within a Few AU of Vega, *ApJ* 736: 14.

Noll, R. (1976). Zernike polynomials and atmospheric turbulence, *Journal of the Optical Society of America* 66(3): 207–211.

Rabbia, Y., Gay, J., Rivet, J.-P. & Schneider, J.-L. (2003). Review of Concepts and Constraints for Achromatic Phase Shifters, *GENIE - DARWIN Workshop - Hunting for Planets*, Vol. 522 of *ESA Special Publication*.

Spronck, J. F. P., Los, J. W. N. & Pereira, S. F. (2008). Compensation and optimization of dispersion in nulling interferometry, *Society of Photo-Optical Instrumentation Engineers (SPIE) Conference Series*, Vol. 7013 of *Society of Photo-Optical Instrumentation Engineers (SPIE) Conference Series*.

Spronck, J. F. P., Los, J. W. N. & Pereira, S. F. (2009). Dispersion in nulling interferometry for exoplanet detection: experimental validation, *Journal of Optics A: Pure and Applied Optics* 11(1): 015510.

Spronck, J. F. P., Schwab, C. & Fischer, D. A. (2010). Fiber-stabilized PSF for sub-m/s Doppler precision at Lick Observatory, *Society of Photo-Optical Instrumentation Engineers (SPIE) Conference Series*, Vol. 7735 of *Society of Photo-Optical Instrumentation Engineers (SPIE) Conference Series*.

Vogt, S. S., Allen, S. L., Bigelow, B. C., Bresee, L., Brown, B., Cantrall, T., Conrad, A., Couture, M., Delaney, C., Epps, H. W., Hilyard, D., Hilyard, D. F., Horn, E., Jern, N., Kanto, D., Keane, M. J., Kibrick, R. I., Lewis, J. W., Osborne, J., Pardeilhan, G. H., Pfister, T.,

Ricketts, T., Robinson, L. B., Stover, R. J., Tucker, D., Ward, J. & Wei, M. Z. (1994). HIRES: the high-resolution echelle spectrometer on the Keck 10-m Telescope, *in* D. L. Crawford & E. R. Craine (ed.), *Society of Photo-Optical Instrumentation Engineers (SPIE) Conference Series*, Vol. 2198 of *Society of Photo-Optical Instrumentation Engineers (SPIE) Conference Series*, p. 362.

Wallner, O. & Leeb, W. (2002). Minimum length of a single-mode fiber spatial filter, *J. Opt. Soc. Am. A* 19: 2445–2448.

Wallner, O., Leeb, W. & Flatscher, R. (2003). Design of spatial and modal filters for nulling interferometers, Vol. 4838 of *Proc. SPIE*, pp. 668–679.

Recent Progress in Optical Fiber Research

Edited by Dr Moh. Yasin

ISBN 978-953-307-823-6

Hard cover, 450 pages

Publisher InTech

Published online 25, January, 2012

Published in print edition January, 2012

This book presents a comprehensive account of the recent progress in optical fiber research. It consists of four sections with 20 chapters covering the topics of nonlinear and polarisation effects in optical fibers, photonic crystal fibers and new applications for optical fibers. Section 1 reviews nonlinear effects in optical fibers in terms of theoretical analysis, experiments and applications. Section 2 presents polarization mode dispersion, chromatic dispersion and polarization dependent losses in optical fibers, fiber birefringence effects and spun fibers. Section 3 and 4 cover the topics of photonic crystal fibers and a new trend of optical fiber applications. Edited by three scientists with wide knowledge and experience in the field of fiber optics and photonics, the book brings together leading academics and practitioners in a comprehensive and incisive treatment of the subject. This is an essential point of reference for researchers working and teaching in optical fiber technologies, and for industrial users who need to be aware of current developments in optical fiber research areas.

InTech Europe
University Campus STeP Ri
Slavka Krautzeka 83/A
51000 Rijeka, Croatia
Phone: +385 (51) 770 447
Fax: +385 (51) 686 166
www.intechopen.com

InTech China
Unit 405, Office Block, Hotel Equatorial Shanghai
No.65, Yan An Road (West), Shanghai, 200040, China
中国上海市延安西路65号上海国际贵都大饭店办公楼405单元
Phone: +86-21-62489820
Fax: +86-21-62489821

IntechOpen